Mitochondrial Colocalization with Ca^{2+} Release Sites is Crucial to Cardiac Metabolism

Asuka Hatano,* Jun-ichi Okada, Takumi Washio, Toshiaki Hisada, and Seiryo Sugiura
Department of Frontier Science, The University of Tokyo, Kashiwa, Chiba, Japan

ABSTRACT In cardiomyocyte subcellular structures, colocalization of mitochondria with Ca^{2+} release sites is implicated in regulation of cardiac energetics by facilitating Ca^{2+} influx into mitochondria to modulate the tricarboxylic acid (TCA) cycle. However, current experimental techniques limit detailed examination of this regulatory mechanism. Earlier, we developed a three-dimensional (3D) finite-element cardiomyocyte model featuring a subcellular structure that integrates excitation-contraction coupling and energy metabolism. Here, using this model, we examined the influence of distance between mitochondria and Ca^{2+} release sites by comparing a normal (50-nm) distance model and a large (200-nm) distance model (LD). The influence of distance was minimal under a low pacing rate (0.25 Hz), but under a higher pacing rate (2 Hz), lower levels of mitochondrial Ca^{2+} and NADH, elevated phosphate, and suppressed force generation became apparent in the LD model. Such differences became greater when functional impairments (reduced TCA cycle activity, uncoupling effect, and failing excitation-contraction coupling) were additionally imposed. We concluded that juxtaposition of the mitochondria and the Ca^{2+} release sites is crucial for rapid signal transmission to maintain cardiac-energy balance. The idealized 3D model of cardiac excitation-contraction and metabolism is a powerful tool to study cardiac energetics.

INTRODUCTION

Recent studies have identified an important role for mitochondrial Ca^{2+} in myocardial energy metabolism by upregulating the tricarboxylic acid (TCA) cycle to stimulate ATP production. Because the rise in cytosolic Ca^{2+} triggers contractions in the sarcomeres—the primary locus of energy consumption—incidental Ca^{2+} flux to mitochondria may constitute a feed-forward regulatory mechanism for rapid and fine tuning of energy balance. However, the high half-maximal effective concentration (EC_{50}; ~10 μM) of mitochondrial Ca^{2+} uniporters poses a question as to whether such a mechanism functions in the face of low cytosolic Ca^{2+} transient (peak value, 1–2 μM) (1,2).

Subcellular cardiomyocyte structures may provide a clue to the answer to this question. Electron micrographic studies of subcellular myocyte structures show that mitochondria occupy the entire space between muscle Z-lines; the ends of mitochondria are located near calcium release units (CaRUs), where L-type Ca^{2+} channels (LCCs) and junctional sarcoplasmic reticulum (JSR) face each other in close proximity (3–7). Upon depolarization of the sarcolemma, Ca^{2+} entry through LCCs induces Ca^{2+} release from the JSR and possibly generates a transiently high Ca^{2+} concentration that exceeds the EC_{50} in this subspace, thereby facilitating Ca^{2+} influx to mitochondria (6,8–13). Because of mitochondrial remodeling and dislocation (e.g., swelling, proliferation, and clustering), loss of cytoskeletal connections have been reported in failing myocardium (8,14–16). Elucidation of subcellular structure and function in both healthy and diseased myocardium is of paramount importance. However, limitations of the available experimental techniques have made it difficult to obtain sufficient information for a thorough understanding of these mechanisms.

We have already developed a three-dimensional (3D) model of cardiomyocytes based on the finite-element method (17–19). In this model, cardiac electrophysiology, contraction, and ATP metabolism localized to specific loci of each organelle, diffusion of Ca^{2+} and energy metabolites, and deformation by sarcomere force generation were simulated in detail with subcellular structures.

In this study, we used this model to study the structure-function relationship of mitochondria in cardiac energy metabolism, with particular focus on the significance of the distance between mitochondria and CaRUs. We found the effect of distance on energetic state to be minimal when myocytes were stimulated at low frequency, but we saw significant differences between the normal and large-distance models in mitochondrial [Ca^{2+}], [NADH], and cytosolic phosphate [Pi] at higher stimulation rates. Simulation results of failing myocytes modeling increased proton leak and depressed TCA cycle activity will also be presented.

MATERIALS AND METHODS

3D cardiomyocyte model

The details of 3D cardiomyocyte models have been reported and validated previously (18,19). Briefly, a segment containing three myofibrils of one sarcomere length, together with the adjacent cell membrane and organelle, were modeled by the finite-element method (Fig. 1 *A*). Subcellular components—including mitochondria, myofibril (A-zone, I-zone, and M-line), JSR, network SR (NSR), surface, and t-tubular sarcolemma—were located at the appropriate finite-element-method nodes to reproduce the anatomical

Submitted July 13, 2012, and accepted for publication December 4, 2012.

*Correspondence: asuka-h@sml.k.u-tokyo.ac.jp

Editor: Andrew McCulloch.

0006-3495/13/01/0496/9 $2.00

http://dx.doi.org/10.1016/j.bpj.2012.12.004

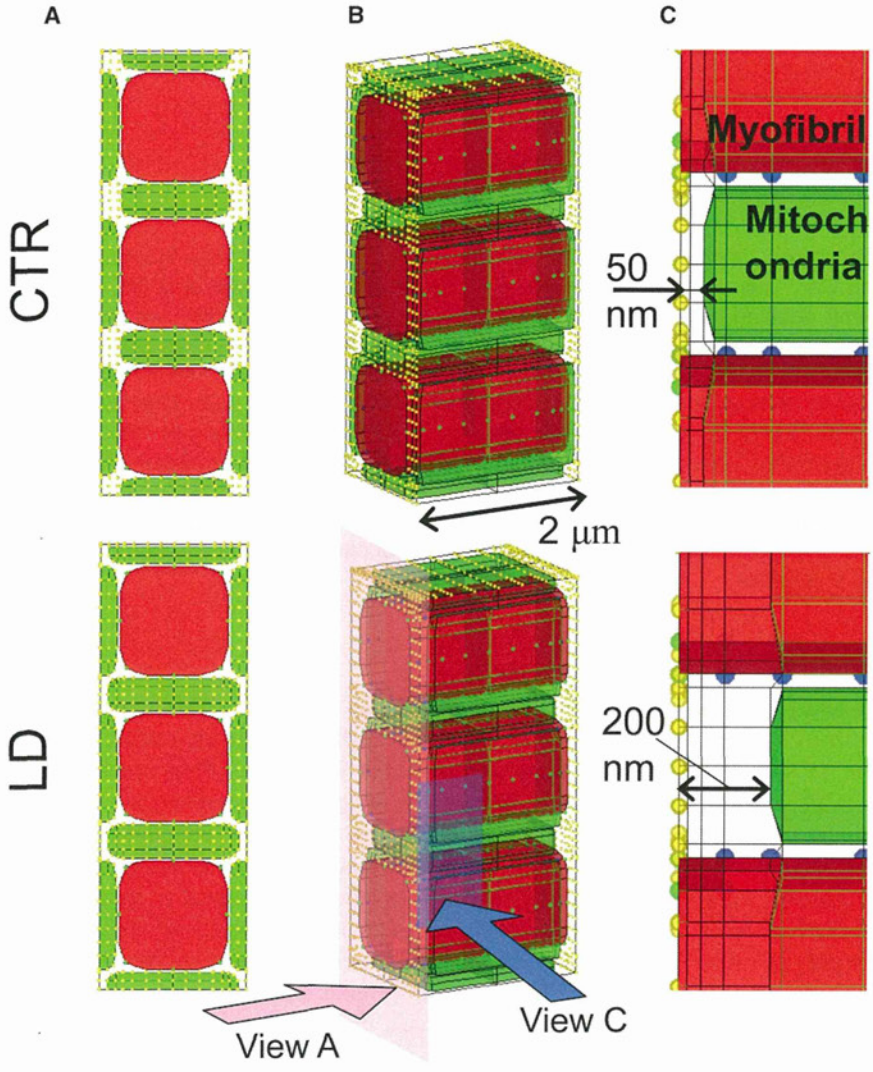

FIGURE 1 Three-dimensional cardiomyocyte models with two different distances between mitochondria and the Ca^{2+} release site: the 50-nm distance model (CTR) (*upper*) and the 200-nm distance model (LD) (*lower*). (*A*) Short-axis views. (*B*) 3D presentations. (*C*) Magnified view of the region near the Ca release sites on the right. Mitochondria are green and myofibrils red. Other subcellular components (channels, pumps, etc.) were assigned to nodes, representing sarcolemma (*yellow*) or SR (*blue*).

structure. Each subcellular component exchanges ions and/or metabolites according to the mathematical formulations expressed as a function of the molecular concentrations in the surrounding cytosol (20,21). These molecules diffuse freely through the cytosolic space; the processes were calculated by solving reaction-diffusion equations. Further details outlining the model can be found in the Supporting Material.

Acto-myosin ATPase model

To examine the influence of metabolic state on the cardiac contraction, we coupled a cross-bridge kinetics model with ATP hydrolysis by myosin (22,23). We adopted a simplified four-state model, schematically shown in Fig. 2 , in which M indicates myosin and A indicates actin. Governing equations are shown in the Appendix, with rate constants taken from the literature (24–27). In this model, [Pi] affects force generation by interfering with the transition from a weakly binding state (A•M•ADP•Pi) to a strongly binding (force-bearing) state (AM•ADP) (28); see also Appendix). Depletion of ATP shifts the distribution into the rigor (AM) state.

The model of Ca^{2+} regulation of contraction was adopted from Rice et al. (29), with parameters refined for guinea pig by Cortassa et al. (20), in which binding of Ca^{2+} to troponin C (TnC) modulates the rate constant of the transition from [A•ATP] to [A•M•ADP•Pi] to cooperatively activate the myofilament. Model equations are shown in the Appendix.

Large-distance model

To investigate the effect of the distance between mitochondria and CaRUs, we created a model with an abnormally large distance (LD) of 200 nm and compared it with a model with a normal-sized 50-nm distance (CTR) (Fig. 1, *A* and *B*). To examine only the effect of the distance between mitochondria and CaRUs, we adjusted the thickness of mitochondria to keep their volume constant in the LD model (Fig. 1 *B*). Accordingly, the volumes of other subcellular structures and the total segment volume were maintained. The normal size, 50 nm, was adopted from electron microscopic observations (8) by taking into account the shrinkage introduced by the fixation procedure (30). The larger size was the maximum value we could attain without changing the volumes of mitochondria, other organelles, and the whole cell.

Failing cardiomyocyte model

Three types of functional abnormality often observed in failing myocardium, i.e., the uncoupling effect (proton leak), depressed TCA cycle activity, and failing excitation-contraction (EC) coupling, were modeled to investigate the influence of distance under diseased conditions. The uncoupling effect was modeled by increasing the proton leak factor, g_H, to 4.0×10^{-5}. The resultant leak flux was comparable to F_0F_1 ATPase

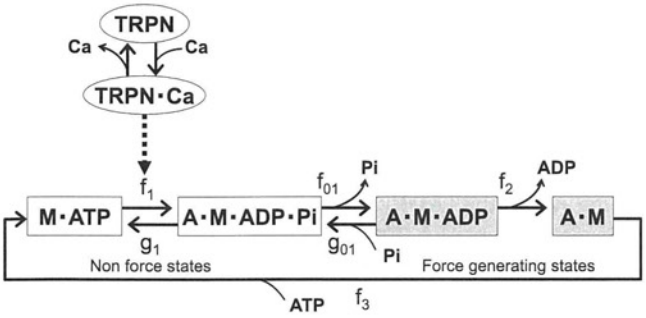

FIGURE 2 State diagrams for the actomyosin ATPase model. A, actin; M, myosin; TRPN, troponin; f_x and g_x, transition rate constants. White boxes correspond to non-force-bearing states. Gray boxes correspond to force-generating states. Transition from M·ATP to A·M·ADP·Pi is cooperatively facilitated by Ca^{2+} binding to troponin. See text for details.

proton flux under pacing at 3 Hz. TCA-cycle activity was depressed by reducing all of the catalytic constants (k_{cat}^{CS}, k_f^{ACO}, k_{cat}^{IDH}, k_{cat}^{KGDH}, k_f^{SL}, k_{cat}^{SDH}, k_f^{FH}, and k_{cat}^{MDH}) by 40%. Failing EC coupling was modeled by decreasing sarcoplasmic Ca^{2+} pump (SERCA) activity (V_{max} 50% of control) and increasing sarcolemmal sodium-calcium exchanger (NCX) activity to 200% of control.

Protocol

Current pulse (100 $\mu A/cm^2$; duration, 0.5 ms) was applied to sarcolemma to simulate electrical pacing. Cardiomyocyte responses to abrupt changes in workload were examined by switching pacing frequency between 0.25 Hz (low load) and 2 Hz (high load) for comparisons with the experimental study (31).

Calculation

All the program codes were written in-house using Fortran language. Computation was performed using an Intel Xeon CPU (3.2 GHz).

RESULTS

Responses of global and local concentrations of Ca^{2+} and metabolites and ion currents of the CTR model were similar to those reported in our previous article (18).

Effect of distance between mitochondria and Ca^{2+} release site

Fig. 3 (*left*) compares the responses of mitochondrial $[Ca^{2+}]$ ($[Ca^{2+}]_{mito}$), [NADH], mitochondrial [ADP] ($[ADP]_{mito}$), and cytosolic [Pi] ($[Pi]_{cyto}$) to abrupt changes in pacing rates between CTR (*black line*) and LD (*gray line*) models. The responses of the CTR model were similar to our previous results (18) and agree with both previous simulation (20) and experimental (31) studies. The LD model showed a similar pattern of responses under the

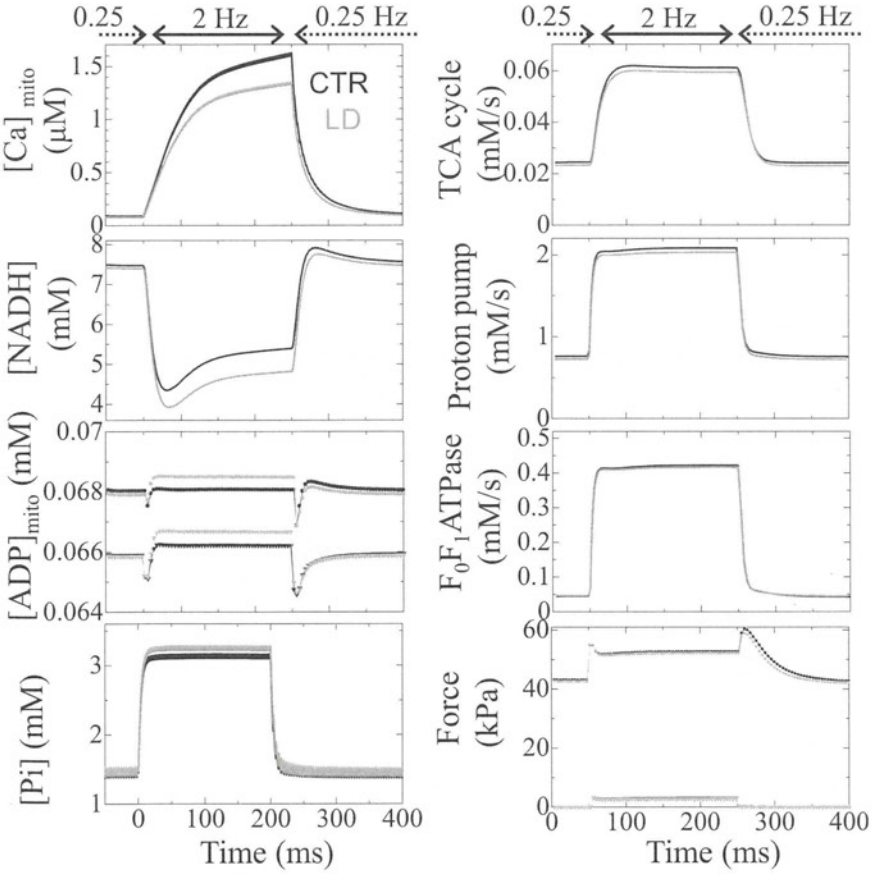

FIGURE 3 Transient responses of the CTR model (*black*) and the LD model (*gray*) to abrupt changes in pacing rate between 0.25 Hz and 2 Hz. (*Left*, *top to bottom*) Mitochondrial Ca^{2+}, NADH, ADP, and cytosolic Pi concentrations. (*Right*, *top to bottom*) Mitochondrial metabolic fluxes for TCA, electron transport chain, and F_0F_1 ATPase, and generated force. In each panel, data averaged over the cytosolic or mitochondrial space are shown. In the graphs of ADP and force, only the maximum (*circles*) and the minimum (*triangles*) values are plotted for visibility.

low-workload condition (0.25 Hz), with levels of $[Ca^{2+}]_{mito}$, [NADH], $[ADP]_{mito}$, and [Pi] close to those observed for the CTR model. However, increasing the workload to 2 Hz introduced significant differences in these parameters. After 200 s of 2-Hz pacing, the respective CTR and LD values were 1.63 and 1.35 μM for $[Ca^{2+}]_{mito}$ (–17% relative change); 5.40 and 4.82 mM for [NADH] (–11%); 39.96 and 40.78 μM for $[ADP]_{mito}$ (+2.1%); and 3.16 and 3.28 mM for [Pi] (+3.6%). The developed force dropped 1.1% in LD compared to CTR; thus, ATP consumption by myofibrils decreased in the LD model (data not shown). We also compared fluxes in metabolic pathways between the two models (Fig. 3, *right*) and found that TCA flux (representing NADH production velocity), electron transport chain flux (NADH consumption velocity), and F_0F_1 ATPase flux (ATP production velocity) were all higher in CTR. Values for CTR versus LD at 200 s after the initiation of 2-Hz pacing were 61.2 and 59.5 μM/s for TCA flux (–2.85% relative change), 2.08 and 2.03 mM/s for electron transport chain flux (–2.57%), and 0.422 and 0.417 mM/s for F_0F_1 ATPase flux (–1.35%). We also note that whereas the responses of electron transport chain flux and F_0F_1 ATPase flux were prompt, the response of the TCA cycle was slow, probably reflecting the slow rise and fall in $[Ca^{2+}]_{mito}$.

Spatiotemporal distributions of $[Ca^{2+}]_{cyto}$ and $[ADP]_{cyto}$ are plotted and compared between 0.25 Hz and 2 Hz in Fig. 4 . The black line indicates the position at 50 nm from the Z-line, and the gray line shows the position at 200 nm. Both $[Ca^{2+}]_{cyto}$ and $[ADP]_{cyto}$ display higher concentrations near the Z-line, but the spatial gradient of $[Ca^{2+}]_{cyto}$ is much larger compared to that of $[ADP]_{cyto}$. Rapid pacing at 2 Hz made this gradient steeper, so that the difference in $[Ca^{2+}]_{cyto}$ between 50 nm and 200 nm became greater. On the other hand, although the 2-Hz pacing raised the $[ADP]_{cyto}$ homogeneously, the difference between 50 nm and 200 nm remained small due to the shallow slope in distribution.

Failing-myocyte models

The effect of distance between mitochondria and Ca^{2+} release site on responses to changing workload was examined in the presence of depressed TCA activity (TCA^-; Fig. 5 , *left*), uncoupling effect (UNC; Fig. 5, *middle*), and failing-EC coupling (EC; Fig. 5, *right*). The first two functional abnormalities (TCA^- and UNC) lowered [NADH] at 0.25 Hz (Fig. 5, *rows 2 and 3*), but phosphorylation potential was relatively constant in both CTR and LD models (data not shown). As seen in the absence of functional abnormalities (Fig. 3), rapid pacing at 2 Hz decreased [NADH] and increased $[ADP]_{mito}$ and [Pi], but these changes were greater. Notably, the differences in [Pi] and force at 2 Hz between CTR and LD models also increased with both TCA^- (+9.0%) and UNC (+6.7%) (Fig. 5, *rows 4 and 5*).

However, the two types of functional abnormalities gave distinct response patterns. Although [NADH] dropped

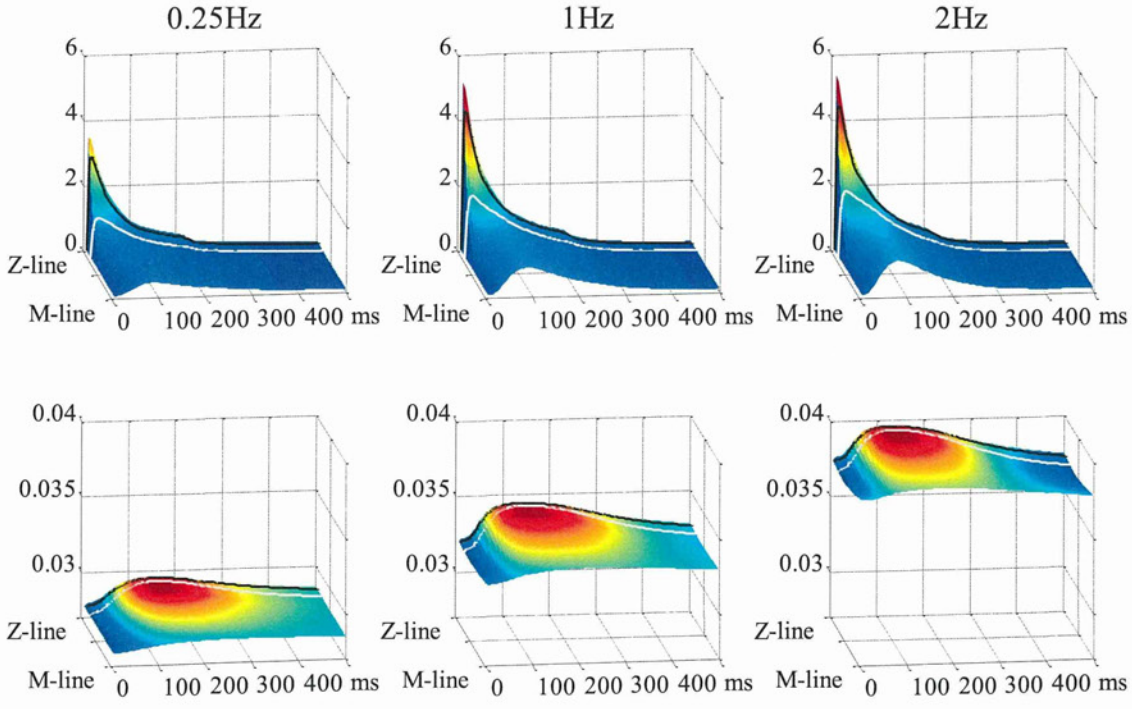

FIGURE 4 Spatiotemporal distributions of cytosolic Ca^{2+} (*upper*) and ADP (*lower*) are shown at pacing rates of 0.25 Hz (*left*), 1 Hz (*middle*), and 2 Hz (*right*). Locations at 50 nm and 200 nm from the Z-line are indicated with black and gray lines, respectively.

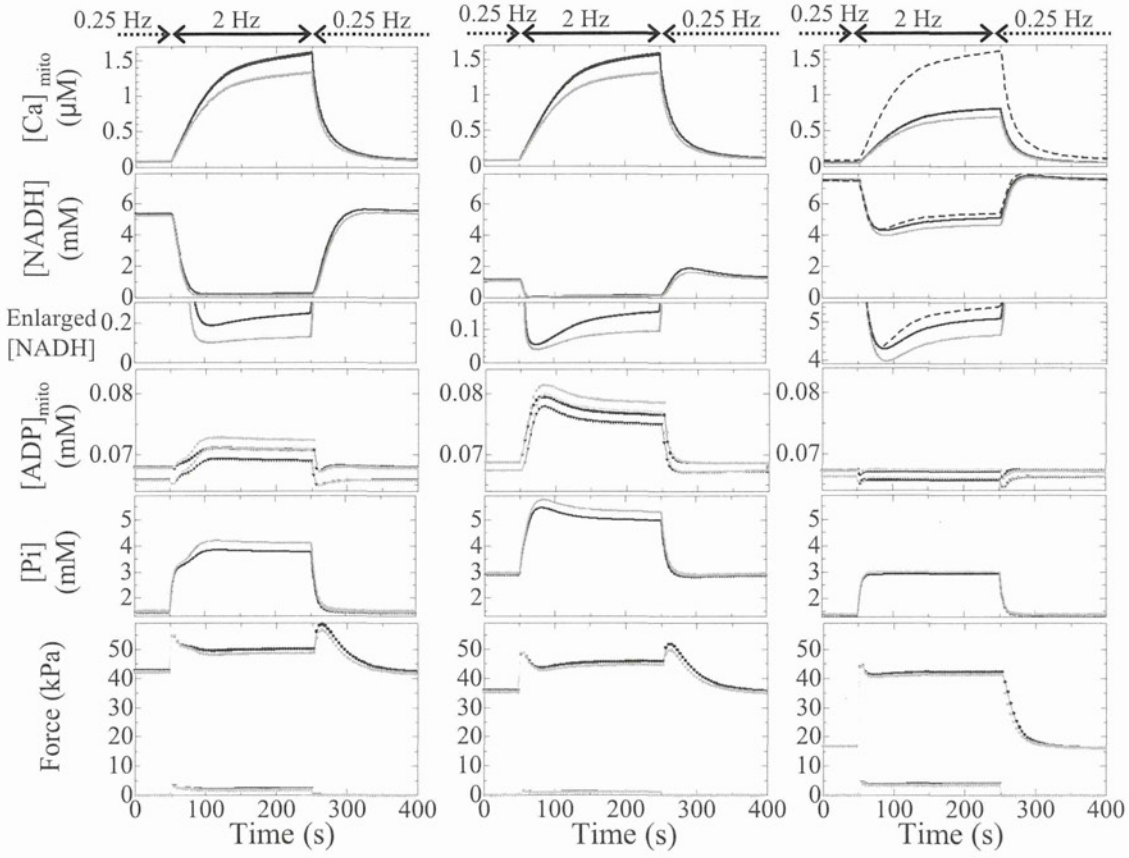

FIGURE 5 Transient responses of the CTR model (*black*) and the LD model (*gray*) under conditions of depressed TCA activity (*left*), uncoupling (*middle*), and failing EC coupling (*right*) with respect to (*top to bottom*) mitochondrial Ca^{2+}, NADH, NADH magnification of bottom parts, mitochondrial ADP, cytosolic Pi, and generated force. Data shown are averaged over the cytosolic or mitochondrial space. In the three upper panels on the right, the responses of the CTR model without functional abnormalities are shown by dashed lines for comparison. In the graphs of ADP and force, only the maximum (*circles*) and minimum (*triangles*) values are plotted for visibility.

acutely upon increasing the pacing rate in both TCA^- and UNC models, [ADP] and [Pi] increased gradually only in TCA^- models. Moreover, closer examination shows that these gradual increases consisted of a rapid first phase and a slow second phase, with differences between CTR and LD becoming apparent in the second phase. In the UNC model, rapid pacing reduced [NADH] to >0.1 mM within 20 s; [ADP] and [Pi] increased rapidly and monotonically to give even overshoots in both CTR and LD models.

On the other hand, the EC model showed unique responses. Reflecting the decreased Ca^{2+} uptake and release of SR, both force level and mitochondrial Ca^{2+} at 2 Hz were low compared to the control (Fig. 5, *right* (*bottom* and *top*, respectively)), but the reduced energy consumption resulting from the impaired force development made the mitochondrial ADP and Pi responses similar to those of control. The response of NADH to the increased pacing rate showed clear contrast to those of the other two models (Fig. 5, *right*). When the distance between mitochondria and CaRU was small, introduction of the EC condition did not change the initial fall in NADH compared to the normal-function model (*dashed line*), but the increase in distance significantly decreased it (–7.5%).

DISCUSSION

In this study, we utilized the 3D integrated cardiomyocyte model we developed earlier (18,19) to examine the significance of distance between CaRUs and mitochondria in cardiac energetics. The simulation study gave us a free hand in setting the experimental conditions and allowed us to focus solely on morphological factors that contribute to cardiac energetics.

Subcellular distributions of metabolites

As in our previous studies (18,19), we identified a steep gradient in $[Ca^{2+}]_{cyto}$, ranging from 10 μM near the CaRUs to 0.1 μM in the M-line region. Such a distribution is consistent with experimental findings (32), and could facilitate mitochondrial Ca^{2+} uptake from the Z-line region. ATP and ADP also showed spatial distributions. Contractile myosin activity hydrolyzes ATP, letting ADP accumulate

in the myofibril A-zone. As M-line-bound creatine kinase (CK) synthesizes ATP from ADP, ADP is distributed homogeneously over the myofibril I zone (Fig. 4) and stimulates mitochondrial ATP synthesis (Fig. S1 and Movie S1 in the Supporting Material); ATP and ADP distribution patterns are complementary. Spatial distributions of other metabolites—creatine, creatine phosphate, and Pi—are negligible because of their high diffusiveness.

Effect of distance between mitochondria and Ca^{2+} release site

The effect of distance can be shown by the differences in cytosolic concentration of signal molecules surrounding the mitochondria. Fig. 6 summarizes the regulatory mechanisms of mitochondrial respiration incorporated in this model. Because ATP is synthesized from ADP by F_0F_1 ATPase, which decreases membrane potential, ATP production is activated in two ways: $[Ca^{2+}]_{mito}$ activates the TCA cycle to produce NADH that is used by the electron transport chain to push up the inner membrane potential (Fig. 6, *red arrows*) and pull up the F_0F_1 ATPase activity by ADP feedback (Fig. 6, *blue arrow*) (20). Because of the distinct distributions of $[Ca^{2+}]_{cyto}$ and $[ADP]_{cyto}$ described above, CTR myocytes can make full use of both these pushing and pulling effects, whereas the LD myocyte cannot. Rapid pacing increases the Ca^{2+} content of the SR and Ca^{2+} release to raise $[Ca^{2+}]_{mito}$, thereby exaggerating the difference in availability of the pushing-up reactants between the CTR and LD models (Fig. 4). On the other hand, because ADP shows fairly flat distribution along the myofibril, even during rapid pacing, the effect of larger distance that emerges under rapid pacing is the pushing-up activation by Ca^{2+}. The decreased pushing-up reactants for the LD model induces lower [NADH] and higher [Pi], resulting in lower force development.

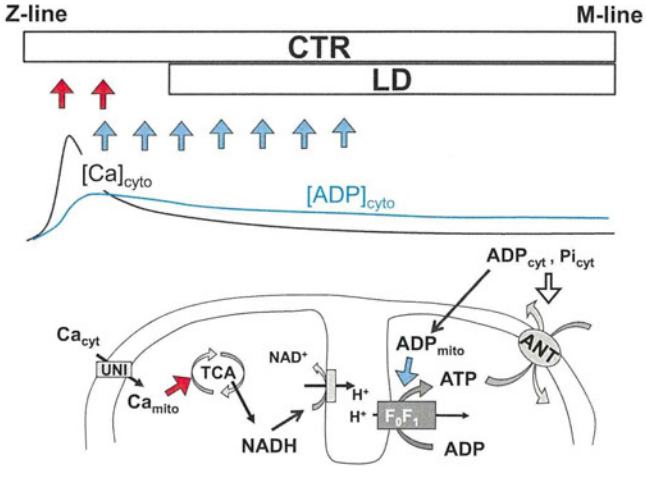

FIGURE 6 Schematic illustrating the effect of distance between mitochondria and the Ca^{2+} release site. (*Upper*) Positions of mitochondria in the CTR and LD models relative to the typical distributions of $[Ca^{2+}]_{cyto}$ and $[ADP]_{cyto}$. (*Lower*) Summary of the mechanisms regulating mitochondrial metabolism incorporated in our model. Red arrows indicate the pushing-up effect and blue arrows the pulling-up effect on mitochondrial membrane potential to facilitate F_0F_1 ATPase. See text for details.

Effect of distance on failing-myocyte models

In diseased myocardium, morphological abnormalities are usually accompanied by functional impairment. Increased levels of mitochondrial uncoupling proteins and decreased mitochondrial efficiency have been reported in heart failure (33). Decreased TCA cycle flux without anaplerosis might also be responsible for the contractile failure (34,35). Both depressed TCA cycle activity and uncoupling decrease the baseline (0.25 Hz) [NADH] level and expand differences in $[ADP]_{mito}$, $[Pi]_{cyto}$, and force between CTR and LD models under high workload. The reason for this enhanced difference is the higher gain of electron transport chain activity to [NADH] when it is <0.5 mM (Fig. 5, *row 3*) (36). Although the depression in force in these failing-myocyte models is still relatively small, its effect in combination with other abnormalities may cause severe disorders in cardiac function.

This response pattern may provide an insight into the mechanism. Depression of the TCA cycle significantly retarded the response to the abrupt change in workload (Fig. 5). Because the TCA cycle plays a central role in the pushing-up mechanism (Fig. 6), the loss of this feed-forward mechanism is expected to slow response, whereas the proton leak reduces the efficiency of ATP synthesis; thus, greater ADP feedback signals are required to meet the higher workload.

We also examined the responses of the failing-EC-coupling model characterized by reduced energy consumption (impaired force generation) and normal mitochondrial function. The initial fall of NADH in response to increased pacing rate was much larger than those of two other disease models but comparable to the normal model. The normally functioning respiratory chain in this model responded even to a small ADP signal to cause the initial fall in NADH (owing to its conversion to NAD^+ for ATP production), but the Ca^{2+}-sensitive pushing-up mechanism (NADH production via the TCA cycle) counteracts this initial fall, depending on the distance between mitochondria and the Ca release site.

Taken together, this simulation study indicated that the effect of the distance between mitochondria and the Ca release site significantly affects regulation of NADH dynamics in response to abrupt change in pacing rate only when both TCA cycle and respiratory chain in mitochondria function normally; the function of EC coupling proteins may not be a dominant factor.

Very recently, Chen et al. (37) studied the role of Mitofusion 2 (Mfn2) protein, which tethers the mitochondria and SR, and found a large initial drop in NADH with

rapid pacing in Mfn2-deficient myocytes compared to the wild-type. Because they did not detect any significant changes in expression and function of EC coupling proteins, despite prominent alterations in mitochondrial SR architecture, they concluded that the physical tethering of SR and mitochondria via Mfn2 is essential for cardiomyocyte bioenergetics feedback response. These experimental results are consistent with those of the simulation study presented here, thus validating our 3D myocyte model.

Study limitation

In this study, due to the limitation in computational power, we had to use a small-scale model that assumed periodicity and symmetry. Therefore, we focused on the effect of distances between mitochondria and CaRUs by changing them uniformly along the t-tubule. Because the configuration of the resultant model was physiologically unrealistic, we performed a simulation on a model in which the distances were periodically different (Fig. A2 *A* in the Appendix). As shown in (Fig. A2 *B*, see figure in the Appendix), however, we could obtain an intermediate result between the control and the uniform large-distance models. A future study using a larger-scale model is necessary to examine the effect of heterogeneous distribution of distances between mitochondria and CaRUs.

CONCLUSION

Our 3D model showed that the small difference in distance between CaRUs and mitochondria could alter metabolic control, reduce robustness to change in workload, and make the cell vulnerable to several pathological conditions. We suggest that juxtaposition of the mitochondria to CaRU is crucial for rapid signal transmission to maintain cardiac energy balance. The 3D integrated model of cardiac EC and metabolism provides a powerful tool for investigating cardiomyocyte physiology in ways not afforded by other experimental methods.

APPENDIX

Equations describing the sarcomere dynamics:

$$\frac{d[A\cdot M\cdot ADP\cdot Pi]}{dt} = -(g_1 + f_{01})[A\cdot M\cdot ADP\cdot Pi] + g_{01}[Pi][A\cdot M\cdot ADP] + f_1[M\cdot ATP] \tag{A1}$$

$$\frac{d[A\cdot M\cdot ADP]}{dt} = -f_2[A\cdot M\cdot ADP] - g_{01}[Pi][A\cdot M\cdot ADP] + f_{01}[A\cdot M\cdot ADP\cdot Pi] \tag{A2}$$

$$\frac{d[A\cdot M]}{dt} = -f_3[A\cdot M] - f_2[A\cdot M\cdot ADP] \tag{A3}$$

$$\frac{d[M\cdot ATP]}{dt} = -f_1[M\cdot ATP] + f_3[A\cdot M] + g_1[A\cdot M\cdot ADP\cdot Pi] \tag{A4}$$

$$\frac{d[LTRPN\cdot Ca]}{dt} = k_p^{ltrpn}\left([LTRPN]_{tot} - [LTRPN\cdot Ca]\right) - k_m^{ltrpn}[LTRPN][Ca] \tag{A5}$$

$$f_1 = f_1^{max}[LTRPN\cdot Ca]^5 \tag{A6}$$

$$f_3 = f_3^{max}\left\{\left(1 + \frac{K_m}{[ATP]}\right)\left(1 + \frac{[ADP]}{K_i}\right)\right\}^{-1} \tag{A7}$$

TABLE A1 Parameter values of acto-myosin ATPase model

Parameter	Value	Unit	Description	Reference
f_{01}	1.2	ms^{-1}	Rate constant from A•M•ADP•Pi to A•M•ADP	(27) [a]
g_{01}^{min}	0.08	$mM^{-1}\ ms^{-1}$	Minimum rate constant from A•M•ADP to A•M•ADP•Pi	(27) [a]
f_1^{max}	0.005	ms^{-1}	Maximum rate constant from M•ATP to A•M•ADP•Pi	
g_1	0.05	ms^{-1}	Rate constant from A•M•ADP•Pi to M•ATP	
f_2	0.004	ms^{-1}	Rate constant from A•M•ADP to A•M	
f_3^{max}	0.9	ms^{-1}	Maximum rate constant for A•M to M•ATP	
K_m	0.03	mM	ATP half-saturation constant	(25)
K_i	0.1	mM	ADP inhibition constant	(26)
$k^{ltrpn}{}_p$	100	ms^{-1}	Ca^{2+} on-rate for troponin low-affinity sites	(20)
$k^{ltrpn}{}_m$	4.0×10^{-2}	$mM^{-1}\ ms^{-1}$	Ca^{2+} off-rate for troponin low-affinity sites	(20)
$[LTRPN]_{tot}$	0.07	mM	Total troponin low-affinity sites	
ζ	0.1	mM^{-1} kPa	Conversion factor normalizing to physiological force	

[a]Parameters were doubled considering the temperature.

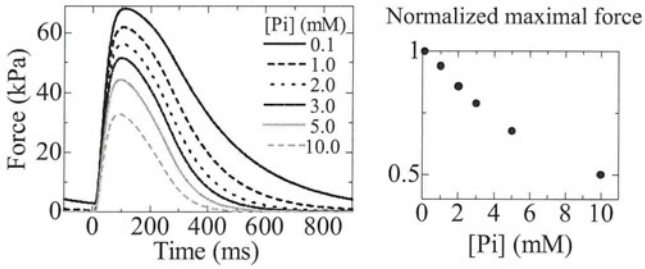

FIGURE A1 (*Left*) Time courses of twitch force under various [Pi] (0.1, 1.0, 2.0, 3.0, 5.0, and 10.0 mM). (*Right*) Normalized maximal twitch force as a function of [Pi].

$$g_{01} = g_{01}^{min}\left(1 + \frac{2.3 - SL}{(2.3 - 1.7)^{1.6}}\right) \quad \text{(A8)}$$

$$\text{Force} = \zeta([A{\cdot}M{\cdot}ADP] + [A{\cdot}M]) \quad \text{(A9)}$$

$$V_{AM} = f_3[A{\cdot}M] \quad \text{(A10)}$$

A, actin; LTRPN, troponin low-affinity sites; M, myosin; SL, sarcomere length; V_{AM}, ATPase rate. Parameters are shown in Table A1 .

Fig. A1 , *left*, shows the isometric twitch force of the CTR model paced at 1 Hz under various [Pi] conditions. Peak twitch force decreases almost linearly with increasing [Pi], and at 10 mM [Pi], the peak twitch force becomes about half of that under 0.1 mM [Pi] (Fig. A2, *right*).

SUPPORTING MATERIAL

Supplemental methods, one figure, and two movies are available at http://www.biophysj.org/biophysj/supplemental/S0006-3495(12)05113-2.

This research was supported by the Japan Society for the Promotion of Science (JSPS) through its Funding Program for World-Leading Innovative R&D on Science and Technology (FIRST Program).

REFERENCES

1. Gunter, T. E., K. K. Gunter, ..., C. E. Gavin. 1994. Mitochondrial calcium transport: physiological and pathological relevance. *Am. J. Physiol.* 267:C313–C339.
2. Sedova, M., E. N. Dedkova, and L. A. Blatter. 2006. Integration of rapid cytosolic Ca^{2+} signals by mitochondria in cat ventricular myocytes. *Am. J. Physiol. Cell Physiol.* 291:C840–C850.
3. Fawcett, D. W., and N. S. McNutt. 1969. The ultrastructure of the cat myocardium. I. Ventricular papillary muscle. *J. Cell Biol.* 42:1–45.
4. Ohata, H., E. Chacon, ..., J. J. Lemasters. 1998. Mitochondrial Ca^{2+} transients in cardiac myocytes during the excitation-contraction cycle: effects of pacing and hormonal stimulation. *J. Bioenerg. Biomembr.* 30:207–222.
5. Csordás, G., A. P. Thomas, and G. Hajnóczky. 2001. Calcium signal transmission between ryanodine receptors and mitochondria in cardiac muscle. *Trends Cardiovasc. Med.* 11:269–275.
6. Lukyanenko, V., A. Chikando, and W. J. Lederer. 2009. Mitochondria in cardiomyocyte Ca^{2+} signaling. *Int. J. Biochem. Cell Biol.* 41:1957–1971.
7. Hayashi, T., M. E. Martone, ..., M. Hoshijima. 2009. Three-dimensional electron microscopy reveals new details of membrane systems for Ca^{2+} signaling in the heart. *J. Cell Sci.* 122:1005–1013.
8. Sharma, V. K., V. Ramesh, ..., S. S. Sheu. 2000. Transport of Ca^{2+} from sarcoplasmic reticulum to mitochondria in rat ventricular myocytes. *J. Bioenerg. Biomembr.* 32:97–104.
9. Bers, D. M. 2002. Cardiac excitation-contraction coupling. *Nature.* 415:198–205.
10. Shannon, T. R., F. Wang, ..., D. M. Bers. 2004. A mathematical treatment of integrated Ca dynamics within the ventricular myocyte. *Biophys. J.* 87:3351–3371.
11. Maack, C., S. Cortassa, ..., B. O'Rourke. 2006. Elevated cytosolic Na^+ decreases mitochondrial Ca^{2+} uptake during excitation-contraction coupling and impairs energetic adaptation in cardiac myocytes. *Circ. Res.* 99:172–182.
12. Belmonte, S., and M. Morad. 2008. "Pressure-flow"-triggered intracellular Ca^{2+} transients in rat cardiac myocytes: possible mechanisms and role of mitochondria. *J. Physiol.* 586:1379–1397.
13. O'Rourke, B., and L. A. Blatter. 2009. Mitochondrial Ca^{2+} uptake: tortoise or hare? *J. Mol. Cell. Cardiol.* 46:767–774.

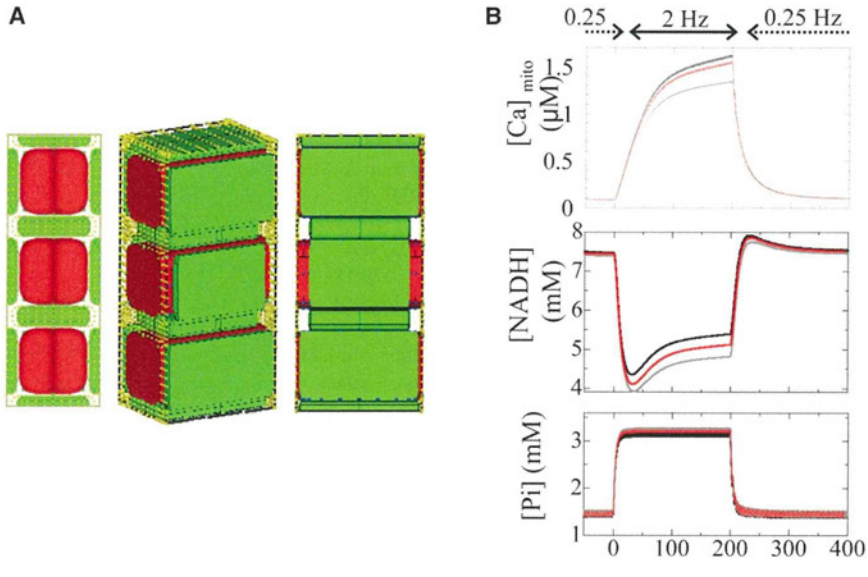

FIGURE A2 (*A*) Model with mixed distances between mitochondria and CaRUs. The distances were adjusted to 50, 200, and 50 nm. (*B*) Reponses of $[Ca]_{mito}$ (*upper*), NADH (*middle*), and Pi (*lower*) to alterations in pacing rate. Black line, control model (distance = 50 nm); gray line, large-distance model (distance = 200 nm); red line, mixed distance.

14. Milner, D. J., M. Mavroidis, ..., Y. Capetanaki. 2000. Desmin cytoskeleton linked to muscle mitochondrial distribution and respiratory function. *J. Cell Biol.* 150:1283–1298.

15. Capetanaki, Y. 2002. Desmin cytoskeleton: a potential regulator of muscle mitochondrial behavior and function. *Trends Cardiovasc. Med.* 12:339–348.

16. Maloyan, A., A. Sanbe, ..., J. Robbins. 2005. Mitochondrial dysfunction and apoptosis underlie the pathogenic process in α-B-crystallin desmin-related cardiomyopathy. *Circulation.* 112:3451–3461.

17. Hatano, A., J. Okada, ..., S. Sugiura. 2011. Juxtaposition of mitochondria to the Ca^{2+} release site is crucial for the cardiac energy balance: a 3-D simulation study of cardiomyocyte. *Trans. Jap. Soc. Med. Biolog. Eng.* 49:829–835.

18. Hatano, A., J. Okada, ..., S. Sugiura. 2011. A three-dimensional simulation model of cardiomyocyte integrating excitation-contraction coupling and metabolism. *Biophys. J.* 101:2601–2610.

19. Hatano, A., J. Okada, ..., S. Sugiura. 2012. Critical role of cardiac t-tubule system for the maintenance of contractile function revealed by a 3D integrated model of cardiomyocytes. *J. Biomech.* 45:815–823.

20. Cortassa, S., M. A. Aon, ..., R. L. Winslow. 2006. A computational model integrating electrophysiology, contraction, and mitochondrial bioenergetics in the ventricular myocyte. *Biophys. J.* 91:1564–1589.

21. Dash, R. K., and D. A. Beard. 2008. Analysis of cardiac mitochondrial Na^{+}-Ca^{2+} exchanger kinetics with a biophysical model of mitochondrial Ca^{2+} handling suggests a 3:1 stoichiometry. *J. Physiol.* 586:3267–3285.

22. Hibberd, M. G., J. A. Dantzig, ..., Y. E. Goldman. 1985. Phosphate release and force generation in skeletal muscle fibers. *Science.* 228: 1317–1319.

23. Goldman, Y. E., and B. Brenner. 1987. Special topic: molecular mechanism of muscle contraction. General introduction. *Annu. Rev. Physiol.* 49:629–636.

24. Kawai, M., Y. Saeki, and Y. Zhao. 1993. Crossbridge scheme and the kinetic constants of elementary steps deduced from chemically skinned papillary and trabeculae muscles of the ferret. *Circ. Res.* 73:33–50.

25. Sugiura, S., H. Yamashita, ..., T. Sugimoto. 1992. Active movement of cardiac myosin on *Characeae* actin cables. *Pflugers Arch.* 421:32–36.

26. Yamashita, H., M. Sata, ..., M. Iizuka. 1994. ADP inhibits the sliding velocity of fluorescent actin filaments on cardiac and skeletal myosins. *Circ. Res.* 74:1027–1033.

27. Araujo, A., and J. W. Walker. 1996. Phosphate release and force generation in cardiac myocytes investigated with caged phosphate and caged calcium. *Biophys. J.* 70:2316–2326.

28. Kusuoka, H., M. Inoue, ..., H. Watari. 1986. Cyclical changes in energy-related metabolites in myocardium detected by phosphorus nuclear magnetic resonance. *In* New Approaches in Cardiac Mechanics. A. H. Kitamura, H. Abe, and K. Sagawa, editors. Routledge, Tokyo. 99–109.

29. Rice, J. J., R. L. Winslow, and W. C. Hunter. 1999. Comparison of putative cooperative mechanisms in cardiac muscle: length dependence and dynamic responses. *Am. J. Physiol.* 276:H1734–H1754.

30. Parfenov, A. S., V. Salnikov, ..., V. Lukyánenko. 2006. Aqueous diffusion pathways as a part of the ventricular cell ultrastructure. *Biophys. J.* 90:1107–1119.

31. Brandes, R., and D. M. Bers. 2002. Simultaneous measurements of mitochondrial NADH and Ca^{2+} during increased work in intact rat heart trabeculae. *Biophys. J.* 83:587–604.

32. Weber, C. R., V. Piacentino, 3rd, ..., D. M. Bers. 2002. Na^{+}-Ca^{2+} exchange current and submembrane $[Ca^{2+}]$ during the cardiac action potential. *Circ. Res.* 90:182–189.

33. Abel, E. D., and T. Doenst. 2011. Mitochondrial adaptations to physiological vs. pathological cardiac hypertrophy. *Cardiovasc. Res.* 90:234–242.

34. Russell, 3rd, R. R., and H. Taegtmeyer. 1991. Changes in citric acid cycle flux and anaplerosis antedate the functional decline in isolated rat hearts utilizing acetoacetate. *J. Clin. Invest.* 87:384–390.

35. Gibala, M. J., M. E. Young, and H. Taegtmeyer. 2000. Anaplerosis of the citric acid cycle: role in energy metabolism of heart and skeletal muscle. *Acta Physiol. Scand.* 168:657–665.

36. Magnus, G., and J. Keizer. 1997. Minimal model of β-cell mitochondrial Ca^{2+} handling. *Am. J. Physiol.* 273:C717–C733.

37. Chen, Y., G. Csordás, ..., C. Maack. 2012. Mitofusin 2-containing mitochondrial-reticular microdomains direct rapid cardiomyocyte bioenergetic responses via interorganelle Ca^{2+} crosstalk. *Circ. Res.* 111:863–875.

ISSN 1349-2365 Int Heart J

International Heart Journal

Volume 54, Number 1
January 2013

Published Bimonthly
by the International Heart Journal Association

Department of Cardiovascular Medicine
Graduate School of Medicine, The University of Tokyo

Discordance of the Areas of Peak Wall Shear Stress and Tissue Stress in Coronary Artery Plaques as Revealed by Fluid-Structure Interaction Finite Element Analysis

A Case Study

Tatsuya ASANUMA,[1] MEnv, Yasutomi HIGASHIKUNI,[2] MD, Hiroshi YAMASHITA,[2] MD, Ryozo NAGAI,[2,3] MD, Toshiaki HISADA,[1] PhD, *and* Seiryo SUGIURA,[1] MD

SUMMARY

Simulation studies have been performed in attempts to elucidate the significance of shear and tissue stresses in the progression and rupture of coronary artery plaques, but few studies have analyzed both stresses simultaneously. We analyzed the distributions of shear stress and tissue stress in a model of coronary artery plaque based on intravascular ultrasound data by fluid-structure interaction finite element analysis under physiological pressure and flow. As shown in previous studies, the region of peak shear stress was observed at the proximal side of the plaque where flow velocity was high but its value was at most 10 Pa. On the other hand, 1000–10,000 times greater tissue stress was located in the stenotic region but the location of peak tissue stress was different from that of shear stress. We also found that stenting not only stabilizes the stented segment but also reduces the stress in the adjacent region. Fluid-structure interaction analysis revealed discordance in the distribution of shear and tissue stresses. These two stresses exert distinct influences on the coronary plaque, rupture of which may occur where tissue stress exceeds the plaque strength, which is weakened by pathological processes triggered by shear stress. (Int Heart J 2013; 54: 54-58)

Key words: Coronary plaque, Finite element method

The pathophysiology of coronary artery disease is significantly influenced by the local interplay between mechanical stimuli and biological responses.[1)] Cyclically changing intramural pressure and flow in the coronary arteries and the motion of vessels accompanying the heart beat (tethering) create a highly heterogeneous mechanical environment, which could account for the spatial distribution of atherosclerotic lesions. Major components of mechanical stimulus (stress) include wall shear stress applied by the blood flowing to the arterial endothelium, tensile stress due to the distension of the vessel wall, and the bending and stretching of the wall resulting from the tethering effect of surrounding tissues. Experimental studies have shown that cyclic changes in shear stress modulate the permeability and proliferation of endothelial cells.[2,3)] Shear stress is also involved in the accumulation of lipids, and inflammatory cell recruitment and adhesion, thus playing a pivotal role in the progression and vulnerability of atherosclerotic plaques.[4-6)] On the other hand, cyclic stretch also induces such changes to initiate the atherosclerotic process[7,8)] and, more importantly, the high stress generated during tissue deformation can be a direct cause of plaque rupture.[9,10)] However, extrapolation of these findings to clinical cases is hampered by the difficulty in performing *in vivo* measurements of these mechanical parameters.

To circumvent this problem, researchers have utilized the numerical simulation to analyze stress and strain distributions in coronary vessels. In these studies, either 2D (transverse section) or 3D morphologies of coronary arteries were modeled as idealized or realistic models based on angiogram, computed tomography (CT), or intravascular ultrasound (IVUS) images[9-16)] to demonstrate that clinically observed sites of prediction for atherosclerotic plaque formation and rupture show close correlations with the distributions of these mechanical parameters. To date, however, most of these studies have evaluated either only wall shear stress (computational fluid dynamics: CFD) ignoring the deformation of vessel wall or only tissue stress (structural analysis) without considering the blood flow because of the complexity and difficulty of the numerical analysis. Coupled analysis of flow dynamics and structural deformation called fluid-structure interaction (FSI) is eagerly needed not only for the accurate estimation of these stresses but because of the close interplay between them in the pathophysi-

From the [1] Department of Human and Engineered Environmental Studies, Graduate School of Frontier Sciences, The University of Tokyo, Chiba, [2] Department of Cardiovascular Medicine, Graduate School of Medicine, The University of Tokyo, Tokyo, [3] Jichi Medical University, Tochigi, Japan.

This work was supported by the Japan Society for the Promotion of Science through its Funding Program for World-Leading Innovative R&D on Science and Technology (FIRST Program).

Address for correspondence: Seiryo Sugiura, MD, Graduate School of Frontier Sciences, The University of Tokyo, 5-1-5 Kashiwanoha, Kashiwa-shi, Chiba 277-8563, Japan.

Received for publication September 24, 2012.
Revised and accepted November 2, 2012.

ology of atherosclerotic plaques.[17] For instance, both wall shear stress and tissue stress are implicated in plaque rupture but their relative contributions should be clarified by FSI analysis in a realistic coronary artery model.

Very recently, the need for and importance of FSI for the analysis of vascular diseases has been recognized, however, the number of applications is still limited, especially to the carotid artery.[17,18] Therefore, in this study, we applied FSI analysis to both blood flow and wall deformation in a realistic coronary artery model based on IVUS images. The obtained distribution of wall shear stress and tissue stress differed significantly, thereby demonstrating the need and importance of FSI analysis.

Case Report

Among the patients who have undergone coronary interventions at The University of Tokyo Hospital, one case, an 83 year old male, was selected and his clinical data were obtained with informed consent. A lesion located in the straight segment was selected. This study protocol was approved by the Institutional Review Board of The University of Tokyo.

IVUS data acquisition and mesh generation: Images of the proximal segment of the left anterior descending artery were recorded by IVUS (Atlantis SR Pro, 2.8F, 40 MHz, Boston Scientific Corporaton/SCIMED, Maple Grove, MN, USA). The transducer was withdrawn using an auto-pullback system at 0.5 mm/s. In this study, 21 slices covering the lesion were used for model construction. The intervals between slices were 0.25 mm or 0.5 mm depending on the morphology of the vessel. Each slice was segmented manually to delineate the lumen, plaque component, and vessel out-boundary. Stent struts were not explicitly segmented but the finite elements cut across by the stent were assigned a hard tissue property. From these data, we constructed the 3-D vessel geometry of the coronary artery segment and blood in the lumen as a finite element model consisting of 20,065 tetrahedral elements using the mesh generation software written in our laboratory.

Fluid-structure interaction analysis: The details of fluid-structure interaction analysis developed in our laboratory have been described elsewhere.[19] Blood flow was assumed to be Newtonian and incompressible. The strain energy function describing the isotropic tissue material properties of the plaque and vessel wall were adopted from the literature[17] with some modifications in parameter values. Governing equations for fluid (blood) and structure (vessel wall) parts were solved simultaneously using the strong coupling method. We prescribed physiological boundary conditions in the following two steps. First, we increased the luminal pressure to 12 kPa (≒ 90 mmHg) to distend the vessel wall. Next, cyclically changing flow (1 Hz, velocity range 0.06 - 0.3 m/second) was applied to the proximal end and a similar pattern of cyclically changing pressure (70 - 110 mmHg) was prescribed at the distal end following the method of Yang, *et al.*[17] All the finite element computer programs were written in our laboratory.

Patient specific model: Figure 1 shows the IVUS images (A) and constructed finite element model (B) of the stented segment of the proximal left anterior descending artery. In this segment, two Xience V stents (Abbott Vascular, IL) (2.75 × 23 mm to the proximal site and 2.5 × 28 mm to the distal site, indicated by the thick double headed arrows) were implanted. To save computational cost, only part of the stented segments was included.

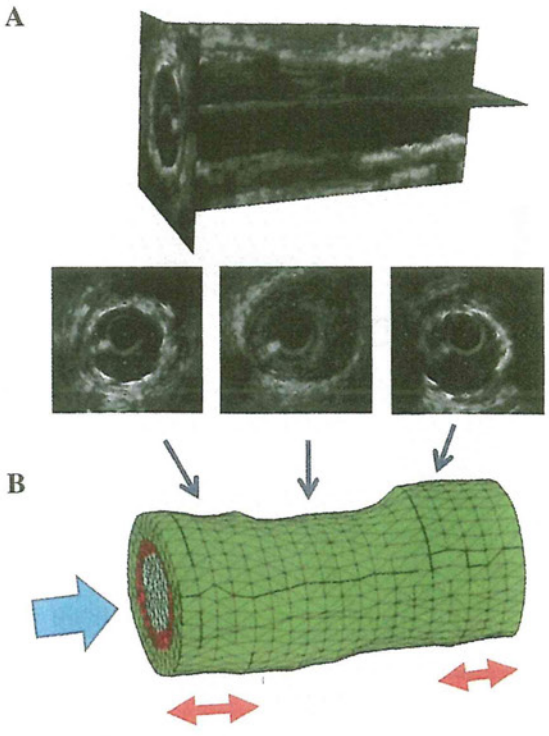

Figure 1. A: Reconstructed IVUS images of the coronary artery segment modeled in this study. Cross-sections of stented segments and the plaque lesion are shown below. **B:** Finite element model. Blood flow was applied from the left end (blue arrow) and pressure was prescribed at the right end. Double headed arrows indicate the stented segments.

Pressure and flow distribution: Figure 2A shows the distribution of flow velocity. Although we applied physiological flow with uniform distribution at the inlet (Figure 2B), the stenosis in the middle disturbed the distribution and a vortex was observed after the stenotic region (Figure 2A inset). Figure 2C shows the pressure prescribed at the outlet. Because the stenosis was not severe in this case, the pressure difference between the inlet and outlet was as small as 0.9 mmHg.

Wall shear stress and tissue stress: Figure 3A shows the distribution of wall shear stress. Similar to earlier studies, high wall shear stress was observed at the stenotic site, where flow velocity was high (Figure 2A). The peak wall shear stress was detected on the proximal side of the plaque but its value was at most 10 Pa. Tissue stress was analyzed in two ways. First, we plotted the intraplaque distribution of von Mises stress (Appendix; Figure 3B), which reflects the shear stress energy often used to determine the yield criterion of steel. Similar to the wall shear stress, a region of high stress was observed at the stenotic region, but its distribution was broad covering the whole circumference. Finally, principal (tensile) stress was plotted as shown in Figure 3C. The maximum tensile stress was found in the stenotic region, but its location was shifted upstream from the location of the maximum wall shear stress. In the thick-walled cylinder structure-like arteries, the direction of tensile stress should be aligned in the circumferential direc-

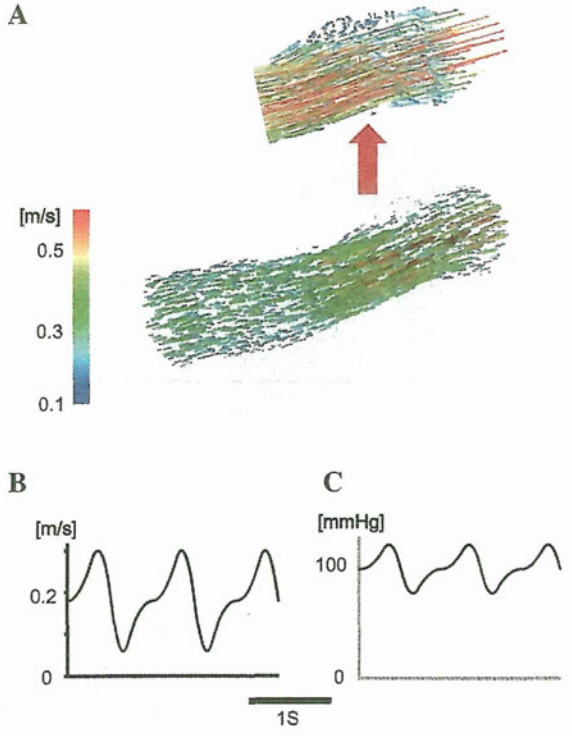

Figure 2. **A:** Flow velocity distribution. The inset shows the magnification of the poststenotic region where a vortex is observed. **B:** Flow velocity applied to the inlet (left). **C:** Prescribed pressure at the outlet (right).

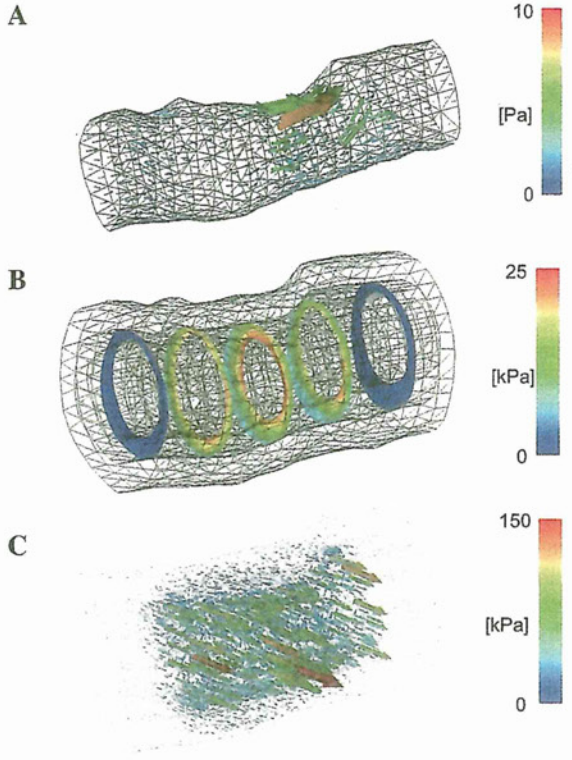

Figure 3. **A:** Distribution of wall shear stress. The mesh indicates the luminal surface. **B:** Distribution of von Mises stress in the plaque. **C:** Distribution of principal (maximum tensile) stress.

tion; however, in this case, it was tilted by 45 degrees or so. The simulation also demonstrated that the tissue stress is 1000 (von Mises stress) to 10,000 (principal stress) times greater than wall stress.

Stenting may reduce the tissue stress: We simulated a case in which stents were not implanted in the arterial segment by changing the material property in the stented region. Figure 4 compares the deformation of the luminal surfaces (upper row) and von Mises stress between the stented (A) and nonstented (B) cases during the cardiac cycle. It is noteworthy that not only the stented region at both ends but also the nonstented middle region was stabilized by stenting as evidenced by the overlapping of black (diastolic) and red (systolic) meshes in the top left panel. As a result, without stents, the von Mises stress increased throughout the segment (Figure 4B).

Discussion

In this study, we analyzed both wall shear stress and tissue stress in a patient specific model of a coronary artery using fluid-structure interaction finite element analysis. Although only one case was analyzed, the results provided us with a unique opportunity to consider the implications of these mechanical factors in the pathophysiology of coronary artery disease.

Fluid-structure interaction analysis: Recent developments in imaging modalities and their applications in clinical cardiology have enabled us to construct a realistic model of coronary arteries. CFD analyses performed on a 3D model of epicardial coronary vessels based on bi-plane angiograms or CT data revealed high wall shear stress on the stenotic site and vortex formation in the distal segment.[16,20,21] A detailed model of the vascular segment based on IVUS images also suggested causal relations between the high wall shear stress and plaque development or rupture.[13,14] In these studies, however, vessel walls were treated as a rigid tube thus totally ignoring their deforma-

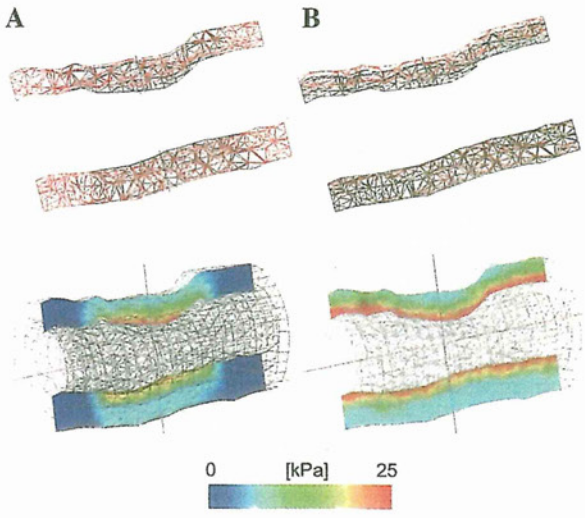

Figure 4. Deformation of the vessel (upper panels) and von Mises stress (bottom panels) in the stented (**A**) and nonstented (**B**) cases during the cardiac cycle. In the upper panels, the black meshes represent the diastolic shape of the vessel and the red meshes represent the systolic shape.

tion due to the pulsatile luminal pressure and cardiac contraction. Another salient feature of IVUS imaging is its capability for tissue characterization. IVUS-based 2D or 3D models of coronary arteries segmented into fibrous plaque, lipid core, and vascular tissue have been used in the stress and/or strain analyses of vascular tissue subjected to intravascular pressure.[9,10,15] Basic and clinical studies have successfully identified the regions of high stress in plaque, which are implicated in the progression and rupture of plaques. However, in these studies, only structural deformation was considered and blood flow was ignored. Considering the fact that wall deformation and blood flow in the vessel are tightly coupled, simulation studies simultaneously solving these two phenomena are needed for an understanding of the pathophysiology of coronary artery disease. To date, however, few studies have analyzed FSI in coronary arteries owing to the difficulty of such an analysis. In one such study, Yang, *et al* modeled a short segment of the right coronary artery of a patient to report the distributions of tissue stress and flow velocity as a preliminary study, but no clinical implications were presented.[17]

Wall shear stress versus tissue stress: One of the main purposes of simulation studies is to identify the mechanical factor responsible for the plaque progression and/or rupture. Whereas the significance of wall shear stress in the progression of atherosclerotic plaque has been widely studied, its causal role in plaque rupture is controversial. Recently, Fukumoto, *et al* reported that high wall shear stress was concentrated in the assumed rupture site in clinical cases.[14] However, as shown in their study as well as ours, the absolute value of wall shear stress is too small to be a direct cause. On the other hand, even in a limited number of cases, Ohayon, *et al* demonstrated coincidence of the area of circumferential tensile peak stress with the location of plaque rupture triggered by balloon angioplasty.[9] Again, we note that both studies calculated only wall shear stress or tissue stress.

Although plaque rupture was not documented, we could evaluate both wall shear stress and tissue stress in a clinical case. Similar to earlier studies, high wall shear stress and tissue stress were concentrated in the plaque region but their distributions differed slightly. This raises the question of which location is at potential risk of rupture? We hypothesize that 1) wall shear stress stimulates various biological processes to make the plaque vulnerable, and 2) plaque rupture takes place where tissue stress exceeds the plaque strength (Figure 5A). The location of plaque rupture does not necessarily coincide with the peak of wall shear stress or tissue stress (Figure 5B). Further studies including many clinical cases with detailed information on the morphology and properties of plaque tissue are needed to validate these hypotheses and make the prediction of rupture risk a possibility in the near future.

Finally, we also found that implantation of stents stabilizes and reduces the deformation of adjacent segments. This finding may help optimize strategies for coronary intervention.

Limitations: Although this was a preliminary study, the use of a single case to construct our model limits the clinical implications of our findings. Follow-up analyses on many cases should be performed in the future. On the technical side, improvement of the modeling method is needed. Firstly, finer segmentation of IVUS images coupled with the proper assignment of a material property to each tissue should be attempted for more accurate evaluation and risk estimation. Second, although reported to be negligible in an earlier study,[17] the bending motion of the vessels by cardiac contraction must be included to simulate the heart under various conditions. Finally, although high performance computing is required, a large scale model including the whole coronary artery tree coupled with a beating heart model will surely help us understand the complex interplay among the tissue deformation and blood flow in the pathogenesis of coronary artery disease.

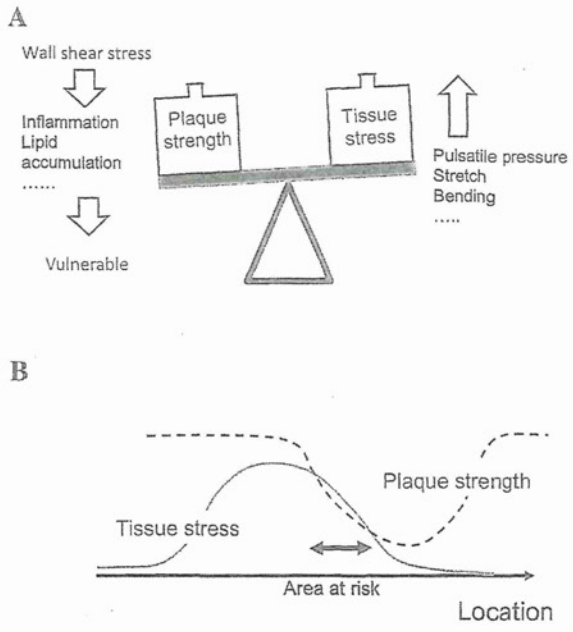

Figure 5. A: Conflicting factors causing plaque rupture **B:** Conceptual diagram showing the area at risk.

Appendix

von Mises stress was calculated by the following equation:

$$\sigma_M = \sqrt{\frac{1}{2}\{(S_{11}-S_{22})^2+(S_{22}-S_{33})^2+(S_{33}-S_{11})^2+3(S_{12}^2+S_{21}^2+S_{23}^2+S_{12}^2+S_{31}^2+S_{32}^2)\}}$$

References

1. Vanepps JS, Vorp DA. Mechano-pathobiology of atherogenesis: a review. J Surg Res 2007; 142: 202-17. (Review)
2. Himburg HA, Grzybowski DM, Hazel AL, LaMack JA, Li XM, Friedman MH. Spatial comparison between wall shear stress measures and porcine arterial endothelial permeability. Am J Physiol Heart Circ Physiol 2004; 286: H1916-22.
3. White CR, Haidekker M, Bao X, Frangos JA. Temporal gradients in shear, but not spatial gradients, stimulate endothelial cell proliferation. Circulation 2001; 103: 2508-13.
4. Chatzizisis YS, Coskun AU, Jonas M, Edelman ER, Feldman CL, Stone PH. Role of endothelial shear stress in the natural history of coronary atherosclerosis and vascular remodeling: molecular, cellular, and vascular behavior. J Am Coll Cardiol 2007; 49: 2379-93. (Review)
5. Helderman F, Segers D, de Crom R, *et al*. Effect of shear stress on vascular inflammation and plaque development. Curr Opin in Lipidol 2007; 18: 527-33. (Review)
6. Ridger V, Krams R, Carpi A, Evans PC. Hemodynamic parameters regulating vascular inflammation and atherosclerosis: a brief up-

date. Biomed Pharmacother 2008; 62: 536-40. (Review)
7. Howard AB, Alexander RW, Nerem RM, Griendling KK, Taylor WR. Cyclic strain induces an oxidative stress in endothelial cells. Am J Physiol 1997; 272: C421-7.
8. Wang DL, Wung BS, Shyy YJ, *et al.* Mechanical strain induces monocyte chemotactic protein-1 gene expression in endothelial cells. Effects of mechanical strain on monocyte adhesion to endothelial cells. Circ Res 1995; 77: 294-302.
9. Ohayon J, Teppaz P, Finet G, Rioufol G. In-vivo prediction of human coronary plaque rupture location using intravascular ultrasound and the finite element method. Coron Artery Dis 2001; 12: 655-63.
10. Imoto K, Hiro T, Fujii T, *et al.* Longitudinal structural determinants of atherosclerotic plaque vulnerability: a computational analysis of stress distribution using vessel models and three-dimensional intravascular ultrasound imaging. J Am Coll Cardiol 2005; 46: 1507-15.
11. Baldewsing RA, de Korte CL, Schaar JA, Mastik F, van der Steen AF. Finite element modeling and intravascular ultrasound elastography of vulnerable plaques: parameter variation. Ultrasonics 2004; 42: 723-9.
12. Versluis A, Bank AJ, Douglas WH. Fatigue and plaque rupture in myocardial infarction. J Biomech 2006; 39: 339-47.
13. Wahle A, Lopez JJ, Olszewski ME, *et al.* Plaque development, vessel curvature, and wall shear stress in coronary arteries assessed by X-ray angiography and intravascular ultrasound. Med Image Anal 2006; 10: 615-31.
14. Fukumoto Y, Hiro T, Fujii T, *et al.* Localized elevation of shear stress is related to coronary plaque rupture: a 3-dimensional intravascular ultrasound study with in-vivo color mapping of shear stress distribution. J Am Coll Cardiol 2008; 51: 645-50.
15. Liang Y, Zhu H, Gehrig T, Friedman MH. Measurement of the transverse strain tensor in the coronary arterial wall from clinical intravascular ultrasound images. J Biomech 2008; 41: 2906-11.
16. De Santis G, Mortier P, De Beule M, Segers P, Verdonck P, Verhegghe B. Patient-specific computational fluid dynamics: structured mesh generation from coronary angiography. Med Biol Eng Comput 2010; 48: 371-80.
17. Yang C, Bach RG, Zheng J, *et al.* In vivo IVUS-based 3-D fluid-structure interaction models with cyclic bending and anisotropic vessel properties for human atherosclerotic coronary plaque mechanical analysis. IEEE Trans Biomed Eng 2009; 56: 2420-8.
18. Teng Z, Canton G, Yuan C, *et al.* 3D critical plaque wall stress is a better predictor of carotid plaque rupture sites than flow shear stress: An in vivo MRI-based 3D FSI study. J Biomech Eng 2010; 132: 031007.
19. Zhang Q, Hisada T. Analysis of fluid-structure interaction problems with structural buckling and large domain changes by ALE finite element method. Comput Methods Appl Mech Engrg 2001; 190: 6341-57.
20. Katritsis DG, Theodorakakos A, Pantos I, *et al.* Vortex formation and recirculation zones in left anterior descending artery stenoses: computational fluid dynamics analysis. Phys Med Biol 2010; 55: 1395-411.
21. Chaichana T, Sun Z, Jewkes J. Computation of hemodynamics in the left coronary artery with variable angulations. Biomech 2011; 44: 1869-78.

34th Annual International Conference of the IEEE EMBS
San Diego, California USA, 28 August - 1 September, 2012

Exercise Training Plus Calorie Restriction Causes Synergistic Protection against Cognitive Decline via Up-regulation of BDNF in Hippocampus of Stroke-prone Hypertensive Rats

T. Kishi, K. Sunagawa

Abstract— **One of the important organ damage of hypertension is cognitive decline. Cognitive function is determined by the function of hippocampus, and previous studies have suggested that the decrease in brain-derived neurotrophic factor (BDNF) in the hippocampus causes cognitive decline. Protection against cognitive decline is reported not only in pharmacological therapy but also in exercise training or calorie restriction. The aim of the present study was to determine whether exercise training plus calorie restriction cause synergistic protection against cognitive decline via BDNF in the hippocampus or not. Exercise training for 28 days improved cognitive decline determined by Morris water maze test via up-regulation of BDNF in the hippocampus of stroke-prone spontaneously hypertensive rats, whereas calorie restriction for 28 days did not. However, exercise training plus calorie restriction causes the protection against cognitive decline to a greater extent than exercise training alone. In conclusion, exercise training plus calorie restriction causes synergistic protection against cognitive decline via up-regulation of BDNF in the hippocampus of stroke-prone hypertensive rats.**

I. Introduction

One of the important organ damages of hypertension and cardiovascular diseases is cognitive decline. Systemic oxidative stress and/or antioxidant deficiency cause cognitive decline [1], and especially, oxidative stress in hippocampus impairs cognitive function [2]. In the brain, brain-derived neurotrophic factor (BDNF) is known to be involved in the protective mechanisms against stress and cell death as an antioxidant [3-5]. In the hippocampus, BDNF protects against ischemic cell damage [6].

Not only the pharmacological therapy but also exercise training [7-9] or calorie restriction [10. 11] has been suggested to cause the protection against cognitive decline. Furthermore, calorie restriction improved cognitive function through the effects on hippocampus. However, in a previous clinical study, calorie restriction and/or exercise training did not protect against cognitive decline [12]. In hypertensive rats, it has not been determined whether calorie restriction protects against cognitive decline or not. The mechanisms in which exercise training and/or calorie restriction cause the protection against cognitive decline should be discussed more.

The aim of the present study was to determine whether exercise training plus calorie restriction causes synergistic protection against cognitive decline via up-regulation of BDNF in the hippocampus of stroke-prone hypertensive rats. To do this aim, we used stroke-prone spontaneously hypertensive rats (SHRSP), as hypertensive and vascular dementia model rats [13]. We divided SHRSP into 4 groups, SHRSP with exercise training (EX), SHRSP with calorie restriction (CR), SHRSP with exercise training plus calorie restriction (E+C), and control SHRSP (Ctl). Exercise training and/or calorie restriction were done for 28 days. Cognitive function was determined by Morris water maze test.

II. Methods

A. Animals

This study was reviewed and approved by the committee on ethics of Animal Experiments, Kyushu University Graduate School of Medical Sciences, and conducted according to the Guidelines for Animal Experiments of Kyushu University. Male SHRSP (12 to 14 week old), weighing 350 to 425 g and fed standard feed were used (SLC Japan, Hamamatsu, Japan). They were housed individually in a temperature-controlled room (22° to 23°C) with a 12-hour/12-hour light-dark cycle (lights on at 7:00 AM). We divided SHRSP into 4 groups, EX, CR, E+C, and Ctl (n=5 for each). Systolic blood pressure was measured dairy using the tail-cuff method (BP-98A; Softron, Tokyo, Japan).

B. Exercise Training

EX and E+C groups were submitted to a maximal exercise test on the treadmill (20 degree angle, 10 m/min for 30 minutes) every day for 28 days, as previously described [14].

C. Calorie Restriction

CR and E+C groups were given 70% of their mean 24-hour food intake. Food was given dairy 2-3 hours before lights off. EX and control groups were free to have food, as previously described [15].

D. Western Blotting Analysis

At the end of the protocol, to obtain the hippocampus tissues, the rats were deeply anesthetized with sodium pentobarbital (100 mg/kg IP) and perfused transcardially with PBS (150 mol/L NaCl, 3 mmol/L KCl, and 5 nmol/L

T. Kishi is with the Department of Advanced Therapeutics for Cardiovascular Diseases, Kyushu University Graduate School of Medical Sciences, Fukuoka 812-8582, Japan (corresponding author to provide phone: +81-92-642-5360; fax: +81-92-642-5374; e-mail: tkishi@cardiol.med.kyushu-u.ac.jp).

K. Sunagawa was with the Department of Cardiovascular Medicine, Kyushu University Graduate School of Medical Sciences, Fukuoka 812-8582, Japan (e-mail: sunagawa@cardiol.med.kyushu-u.ac.jp).

978-1-4577-1787-1/12/$26.00 ©2012 IEEE

phosphate; pH 7.4, 4°C). The brains were removed quickly, and sections 1 mm thick were obtained with a cryostat at −7±1°C. The hippocampus defined according to a rat brain atlas and obtained by a punch-out technique, and the hippocampus tissues were homogenized and then sonicated in a lysing buffer containing 40 mmol/L HEPES, 1% Triton X-100, 10% glycerol, and 1 mmol/L phenylmethanesulfonyl fluoride. The tissue lysate was centrifuged at 6000 rpm for 5 minutes at 4°C with a microcentrifuge. The lysate was collected, and protein concentration was determined with a BCA protein assay kit (Pierce). An aliquot of 20 μg of protein from each sample was separated on 12% SDS-polyacrylamide gel. Proteins were subsequently transferred onto polyvinylidene difluoride membranes (Immobilon-P membrane; Millipore). Membranes were incubated for 2 hours with a rabbit polyclonal antiserum against BDNF (1:1000; Abcam, Cambridge, UK) or α-tubulin (1:1000; Cell Signaling). Membranes were then washed and incubated with a horseradish peroxidase–conjugated horse anti-mouse IgG antibody (1:10000) for 40 minutes. Immunoreactivity was detected by enhanced chemiluminescence autoradiography (plus Western blotting detection kit; Amersham), and was expressed as the ratio to β-tubulin protein.

E. Morris Water Maze Test

Spatial leaning and memory function of the rats were investigated with the Morris water maze test in a circular pool filled with water at a temperature of 25.0±1°C [16]. In the hidden platform test, a transparent platform was submerged 1cm below the water level. Swimming paths were tracked with a camera fixed on the ceiling of the room and stored in a computer. All the procedures of the Morris water maze were performed for 7 days. A pre-training session was carried out at day 0, in which animals were given 60 seconds free swimming without the platform. In the hidden-platform test for 4 days, the rats were given 2 trials (1 session) on day 1 and 4 trials (2 sessions) per day on day 2, 3, and 4. The initial trial interval was about 30 min and the inter-session interval was 2 hours. During each trial, the rats were released from four pseudo-randomly assigned starting points and allowed to swim for 60 seconds. After mounting the platform, the rats were allowed to remain there for 15 seconds, and were then placed in the home cage until the start of the next trial. If a rat was unable to find the platform within 60 seconds, it was guided to the platform and allowed to rest on the platform for 15 seconds. Probe trials were performed at day 5. In the probe trial, the hidden platform was removed and the rats was released from the right quadrant and allowed to swim freely for 60 seconds. The time spent in the target quadrant, where the platform has been located during training, and the time spent in the other quadrants were measured. In the visible-platform test was performed at day 6, the platform was elevated above the water surface and placed in a different position. The rats were given for trials with an inter-trial interval of 10 minutes.

F. Statistical Analysis

All values are expressed as mean ± SEM. Comparisons between any two mean values were performed using Bonferroni's correction for multiple comparisons. ANOVA was used to compare all the parameters in all groups. Differences were considered to be statistically significant at a P value of <0.05.

III. RESULTS

A. Blood Pressure

Systolic blood pressure was reduced to the similar levels in EX and E+C, and was significantly lower in EX and E+C than in Ctl (Fig. 1). Systolic blood pressure was not different between in CR and Ctl (Fig. 1).

B. BDNF in the Hippocampus

The expression of BDNF in the hippocampus was significantly higher in E+C than in Ctl to a greater extent than in EX (Fig. 2). However, the expression of BDNF in the hippocampus was not different between in CR and Ctl (Fig. 2).

C. Morris Water Maze Test

In the hidden platform test, escape latency was significantly lower in E+C than in Ctl to a greater extent than in EX (Fig. 3A). However, escape latency was not different in CR and Ctl (Fig. 3A). In the probe test, E+C resulted in significantly more time in the target quadrant as compared with EX, CR, and Ctl (Fig. 3B). In the visible platform test, there were no significant differences in escape latency among all of the groups.

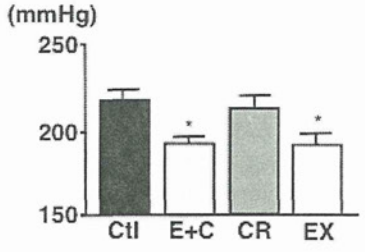

Figure 1. Systolic blood pressure in each groups. *P<0.05 versus Ctl, n=5 for each. Abbreviations; Ctl, control; E+C. exercise training+calorie restriction; CR, calorie restriction; EX, exercise training.

IV. DISCUSSION

In the present study, we demonstrated that exercise training plus calorie restriction improves cognitive performance and increases BDNF in the hippocampus of SHRSP to a greater extent than exercise training alone. However, calorie restriction alone did not have such effects.

These results suggest that exercise training plus calorie restriction might cause synergistic protection against cognitive decline via up-regulation of BDNF in the hippocampus of SHRSP.

It has already demonstrated that exercise training cause the protection against cognitive decline via up-regulation of BDNF in the hippocampus [7, 8]. The results obtained in the present study were compatible to these previous studies. A previous study indicates that superoxide induces down-regulation of BDNF via phosphorylation of cAMP response element binding protein [17]. We have demonstrated that angiotensin II type 1 receptor-induced superoxide is increased in the brain of SHRSP [18], and exercise training reduces superoxide in the brain of SHRSP [14]. Several previous studies have demonstrated that the exercise training inhibits the brain renin-angiotensin system including angiotensin converting enzyme (ACE), ACE2, angiotensin II, angiotensin- (1-7), and their receptors [19-21]. Furthermore, one of the important activating factors of brain renin-angiotensin system is the inflammatory cascade [22], and exercise training is known to lower the inflammatory substances in the brain of rats [23]. We consider that the exercise training-induced anti-inflammation, anti-oxidant, and inhibition of brain renin-angiotensin system cause the up-regulation of BDNF in the hippocampus, which contribute to the protection against cognitive decline.

Interestingly, in the present study, exercise training plus calorie restriction improved the cognitive performance and increases BDNF in the hippocampus to a greater extent than exercise training alone in spite of the similar depressor effects, whereas calorie restriction alone did not cause such effects. We consider that these results involve two findings. First, exercise training-induced protection against cognitive decline is independent of its depressor effect. Second, exercise training plus calorie restriction causes synergistic

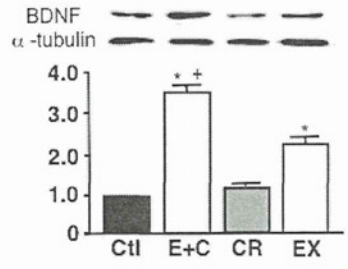

Figure 2. Expression of BDNF in the hippocampus in each group. BDNF / α-tubulin expression was expressed relative to that in Ctl, which was assingned a value of 1. *P<0.05 versus Ctl, +P<0.05 in E+C versus EX, n=5 for each. Abbreviations; Ctl, control; E+C. exercise training+calorie restriction; CR, calorie restriction; EX, exercise training.

protection effect against cognitive decline. Previously, we have demonstrated that exercise training inhibits sympathetic nervous system activation via reduction of oxidative stress in the brain of SHRSP [14]. Furthermore, we also have demonstrated that calorie restriction inhibits sympathetic nervous system activation via reduction of oxidative stress in the brain of dietary-induced obesity rats [15]. These previous results suggest that exercise training or calorie restriction could affect the brain. Although the mechanism in which calorie restriction inhibits oxidative stress in the brain could not been determined in the present study, we hypothesize that calorie restriction may improve adipocytes, inhibit central renin-angiotensin system, directly inhibit oxidative stress in the brain. Circulating angiotensin II acts at circumventricular organs to subsequently activate complex pathways, including those using central angiotensin II as a neurotransmitter, to increases sympathetic outflow [24]. We consider that calorie restriction also reduce oxidative stress in the hippocampus through these mechanisms, and causes the synergistic effect to exercise training. However, it is necessary to do further examination.

To determine the cognitive function, we performed Morris water maze test in the present study, instead of the shuttle avoidance test so that we could focus on hippocampus function. A spatial working memory task, such as Morris water maze test, depends on hippocampus function [25, 26]. Moreover, we used SHRSP as a hypertension and cerebrovascular disease model, and examined the cognitive function by only Morris water maze test. We must do further examination with regard to other cognitive functions in other models, such as Alzheimer, diabetic, and aging.

There are several study limitations in the present study. First, we did not determine the strength and the physiological benefits of the exercise training, such as body weights, lactate level and maximum O_2 consumption. Second, we did not check the calorie restriction-induced changes in metabolism. We did not clarify the cause-and-effect between exercise training/calorie restriction and cognitive function due to these limitations. We have to perform the further studies.

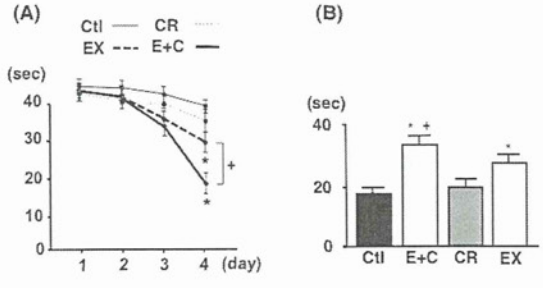

Figure 3. (A) Escape latency time in each group, (B)Time in the target quadrant in each group. *P<0.05 versus Ctl, +P<0.05 in E+C versus EX, n=5 for each. Abbreviations; Ctl, control; E+C. exercise training+calorie restriction; CR, calorie restriction; EX, exercise training.

V. Conclusion

Exercise training plus calorie restriction causes synergistic protective effect against cognitive decline via up-regulation of BDNF in the hippocampus of SHRSP. These results indicate that both exercise training and calorie restriction should be done to the patients with hypertension for the protection against cognitive decline in addition to the pharmacological therapy.

APPENDIX

None.

ACKNOWLEDGMENT

THIS WORK WAS SUPPORTED BY A GRANT-IN-AID FOR SCIENTIFIC RESEARCH FROM THE JAPAN SOCIETY FOR THE PROMOTION OF SCIENCE (22790709).

REFERENCES

[1] Berr C, Balansard B, Arnaud J, Roussel AM, Alperovitch A, "Cognitive decline is associated with systemic oxidative stress: the EVA study. Etude du Vieillissement Arterial," *J Am Geriatr Soc*, 2000, vol. 48, pp. 1285-1291.

[2] Sato H, Takahashi T, Sumitani K, Takatsu H, Urano S, "Glucocorticoid generates ROS to induce oxidative injury in the hippocampus, leading to impairment of cognitive function of rats," *J Clin Biochem Nutr*, 2010, vol. 47, pp. 224-232.

[3] Mancias M, Dwornik A, Ziemlinska E, Fehr S, Schachner M, Czarkowska-Bauch J, Skup M, "Locomotor exercise alters expression of pro-brain-derived neurotrophic factor, brain-derived neurotrophic factor and its receptor TrkB in the spinal cord of adult rats," *Eur J Neurosci*, 2007, vol. 25, pp. 2425-2444.

[4] Zacchigna S, Lambrechts D, Carmeliet P, "Neurovascular signaling defects in neurodegeneration. *Nat Rev*, 2008, vol. 9, pp. 169-181.

[5] Lee TH, Yang JT, Kato H, Wu JH, "Hypertension downregulates the expression of brain-derived neurotrophic factor in the ischemic-vulnerable hippocampal CA1 and cortical areas after carotid artery occlusion," *Brain Res*, 2006, vol. 1116, pp. 31-38.

[6] Beck T, Lindholm D, Castren E, Wree A, "Brain-derived neurotrophic factor protects against ischemic cell damage in rat hippocampus," *J Cereb Blood Flow Metab*, 1994, vol. 14, pp. 689-692.

[7] Liu YF, Chen HI, Wu CL, Kuo YM, Yu L, Juang AM, Wu FS, Chuang JI, Jen CJ, "Differential effects of treadmill running and wheel running on spatial or aversive learning and memory: roles of amygdalar brain-derived neurotrophic factor and synaptotagmin I," *J Physiol*, 2009, vol. 586, pp. 3221-3231.

[8] Kim H, Heo HI, Kim DH, Ko IG, Lee SS, Kim SE, Kim TW, Ji ES, Kim JD, Shin MS, Choi YW, Kim CJ, "Treadmill exercise and methylphenidate ameliorate symptoms of attention deficit/hyperactivity disorder through enhancing dopamine synthesis and brain-derived neurotrophic factor expression in spontaneously hypertensive rats," *Neurosci Lett*, 2011, vol. 504, pp. 35-39.

[9] Gomez-Pinilla F, Vaynman S, Ying Z, "Brain-derived neurotrophic factor functions as a metabotrophin to mediate the effects of exercise on cognition," *Eur J Neurosci*, 2008, vol. 28, pp. 2278-2287.

[10] Wu P, Shen Q, Dong S, Xu Z, Tsien JZ, Hu Y, "Calorie restriction ameliorates neurodegenerative phenotypes in forebrain-specific presenilin-1 and presenilin-2 double knockout mice," *Neurobiol Aging*, 2008, vol. 29, pp.1502-1511.

[11] Yilmaz N, Vural H, Yilmaz M, Sutcu R, Sirmali R, Hicyilmaz H, Delibas N, "Calorie restriction modulates hippocampal NMDA receptors in diet-induced obese rats," *J Recept Signal Transduct Res*, 2011, vol. 31, pp. 214-219.

[12] Martin CK, Anton SD, han H, York-Crowe E, Redman LM, Ravussin E, Williamson DA, "Examination of cognitive function during six months of calorie restriction: results of a randomized controlled study," *Rejuvenation Res*, 2007, vol. 10, pp. 179-190.

[13] Kimura S, Saito H, Minami M, Togashi H, Nakamura N, Nemoto M, Parvez HS, "Pathogenesis of vascular dementia in stroke-prone spontaneously hypertensive rats," *Toxicology*, 2000, vol. 153, pp. 167-178.

[14] Kishi T, Hirooka Y, Katsuki M, Sunagawa K, "Exercise training inhibits sympathetic nerve activity via blockade of AT_1 receptor in the rostral ventrolateral medulla of hypertensive rats," *Clin Exp Hypertens*, to be published.

[15] Kishi T, Hirooka Y, Ogawa K, Konno S, Sunagawa K, "Calorie restriction inhibits sympathetic nerve activity via anti-oxidant effect in the rostral ventrolateral medulla of obesity-induced hypertensive rats," *Clin Exp Hypertens*, 2011, vol. 33, pp. 245-250.

[16] Morris R, "Development of a water-maze procedure for studying spatial learning in the rat," *J Neurosci Methods*, 1984, vol. 11, pp. 47-60.

[17] Chan SH, Wu CW, Chang AY, Hsu KS, Chan JY, "Transcriptional upregulation of brain-derived neurotrophic factor in rostral ventrolateral medulla by angiotensin II: significant in superoxide homeostasis and neural regulation of arterial pressure," *Circ Res*, 2010, vol. 107, pp. 1127-1139.

[18] Kishi T, Hirooka Y, Konno S, Ogawa K, Sunagawa K, "Angiotensin II type 1 receptor-activated caspase-3 through ras/mitogen-activated protein kinase-extracellular signal-regulated kinase in the rostral ventrolateral medulla is involved in sympathoexcitation in stroke-prone spontaneously hypertensive rats," *Hypertension*, 2010, vol. 55, pp. 291-297.

[19] Mousa TM, Liu D, Cornish KG, Zucker IH, "Exercise training enhances baroreflex sensitivity by an angiotensin II-dependent mechanism in chronic heart failure," *J Appl Physiol*, 2008, vol. 104, pp. 616-624.

[20] Kar S, Gao L, Zucker IH, "Exercise training normalizes ACE and ACE2 in the brain of rabbits with pacing-induced heart failure," *J Appl Physiol*, 2010, vol. 108, pp. 923-932.

[21] Felix JVC, Michelini LC, "Training-induced pressure fall in spontaneously hypertensive rats is associated with reduced angiotensinogen mRNA expression within the nucleus tractus solitarii," *Hypertension*, 2007, vol. 50, pp. 780-785.

[22] Chennaoui M, Drogou C, Gomez-Merino D, "Effects of physical training on IL-1β, IL-6 and IL-1ra concentrations in various brain areas of the rat," *Eur Cytokine Netw*, 2008, vol. 19, pp. 8-14.

[23] Francis J, Chu Y, Johnson AK, Weiss RM, Felder RB, "Acute myocardial infarction induces hypothalamic cytokine synthesis," *Am J Physiol*, 2004, vol. 286, pp. H2264-H2271.

[24] Ferguson AV, Washburn DL, "Angiotensin II: a peptidergic neurotransmitter in central autonomic pathways," *Prog Neurobiol*, 1998, vol. 54, pp. 169-192.

[25] Moser MB, Trommald M, Andersen P, "An Increase in dendritic spine density on hippocampal CA1 pyramidal cells following spatial learning in adult rats suggests the formation of new synapses," *Proc Natl Acad Sci U S A*, 1994, vol. 91, pp. 12673-12675.

[26] McHugh TJ, Blum KI, Tsien JZ, Tonegawa S, Wilson MA, "Impaired hippocampal representation of space in CA1-specific NMDAR1 knockout mice," *Cell*, 1996, vol. 87, pp. 1339-1349.

INTERNAL MEDICINE

□ ORIGINAL ARTICLE □

Leg Heating Using Far Infra-red Radiation in Patients with Chronic Heart Failure Acutely Improves the Hemodynamics, Vascular Endothelial Function, and Oxidative Stress

Shujiro Inoue[1], Masao Takemoto[1], Akiko Chishaki[2], Tomomi Ide[1], Mari Nishizaka[1], Mami Miyazono[2], Hiroyuki Sawatari[2] and Kenji Sunagawa[1]

Abstract

Background Systemic thermal therapy (STT) has been associated with beneficial effects in patients with chronic heart failure (CHF). The fact, however, that it requires a dedicated as well as spacious facility and trained personnel makes it difficult to practice in the daily care of patients with CHF.

Objective The aim of this study was to determine whether the leg thermal therapy (LTT) has a positive impact similar to that of STT in patients with CHF.

Methods and Results Twenty patients with CHF (57±17 years old, left ventricular ejection fraction=30±10%) received LTT (45℃) for 20 minutes. Immediately after the treatment, the core temperature had increased (+0.3±0.3℃) ($p<0.01$). While the LTT had no significant effects on the heart rate, systolic arterial pressure, and diastolic blood pressure, it increased the cardiac output (mixed venous oxygen saturation; +2±3%) and decrease the pulmonary capillary wedge pressure (-2±2 mmHg). The LTT significantly improved the flow-mediated vasodilatation (FMD) from 4.8±2.6 to 7.1±3.6%, the antioxidative markers, thiol from 4.0±0.7 to 4.5±0.9 μmoL/g, and the marker of oxidative deoxyribonucleic acid (DNA) damage, urine 8-hydroxy-2'deoxyguanosine (8OHdG) from 100 to 82±3%, respectively ($p<0.05$). No patient had any adverse effects associated with LTT.

Conclusion LTT acutely improved FMD, and oxidative stress in patients with CHF. Although the long-term effect of LTT remains to be investigated, its practicality which is comparable to that of STT would make it an attractive therapeutic strategy for patients with CHF.

Key words: heart failure, thermal therapy, endothelial function, oxidative stress

(Intern Med 51: 2263-2270, 2012)
(DOI: 10.2169/internalmedicine.51.7115)

Introduction

Systemic thermal therapy (STT), so-called Sauna or warm water insertion therapy (1), which is considered to be one of the thermal vasodilatation therapies and has been applied to many healthy people for centuries, has been gathering attention from various medical fields. There have been reviews of the physiologic effects, benefits and risks of sauna bathing (2, 3). It seems that the risks of sauna have been emphasized in people without chronic heart failure (CHF) (4), and thus many patients with CHF do avoid sauna because of those risks or adverse effects. However, sauna bathing may be a beneficial therapeutic option for patients with hypertension, CHF, or coronary artery disease (5-8). The common mechanism of the action might be improvement in vascular endothelial function which results in a reduced cardiac preload and afterload (2).

Tei and colleagues have introduced a supervised dry sauna at 60℃ and have shown that hyperthermia appeared

[1]Department of Cardiovascular Medicine, Kyushu University Hospital, Japan and [2]Department of Health Sciences, Kyushu University Graduate School of Medical Sciences, Japan
Received for publication December 16, 2011; Accepted for publication April 1, 2012
Correspondence to Dr. Masao Takemoto, matakemo@cardiol.med.kyushu-u.ac.jp